COMMUNICATION

ADVANCED MATERIALS INTERFACES
www.advmatinterfaces.de

Resolving Nanocomposite Interfaces via Simultaneous Submicrometer Optical-Photothermal Infrared-Raman Microspectroscopy

Alexander J. Wang, Eoghan P. Dillon, Surendra Maharjan, Kang-Shyang Liao, Brian P. McElhenny, Tian Tong, Shuo Chen, Jiming Bao, and Seamus A. Curran*

Nanocomposite materials are assuming increasingly important roles across contemporary materials science. Analytical characterizations and visualizations of nanoscale interphases/interfaces are critical to development of novel multiphase nanostructures and nanoscale systems. While conventional vibrational spectroscopies are indispensable physicochemical characterization tools, standard techniques such as Fourier-transform and quantum cascade laser infrared (IR) microspectroscopies are intrinsically limited in spatial resolution by the wavelength-dependent diffraction limit of IR light (≈5–12 µm). Optical-photothermal infrared (O-PTIR) with simultaneous hyperspectral Raman microspectroscopy (O-PTIR+R) is a novel all-optical technique that circumvents such diffraction limits, yielding position-specific IR spectra with sub-micrometer wavelength-independent resolution across the mid-IR. This work implements single-frequency O-PTIR with concomitant hyperspectral Raman microspectroscopy to resolve interfacial regions in a poly(octadecyl acrylate)-*grafted*-multiwall carbon nanotube (PODA-*g*-MWCNT) nanocomposite for wearable temperature sensors and highlights how the O-PTIR+R technique can be used for analytical characterization and visualization of other nanocomposite systems below resolution limitations of conventional IR spectroscopies.

Development and optimization of multiphase nanoscale systems and functional nanoarchitectures require a meticulous physicochemical understanding of interfacial regions and their interactions. Disordered multiphase systems like polymer nanocomposites often exhibit intricate and convoluted interfacial regions across interphases.[1–4] Resolving such nanocomposite interphases with sub-micrometer resolution and chemical exactitude is of substantial importance towards a complete quantitative understanding of nanoscale systems.[5] Vibrational spectroscopies afford the most chemical specificity, but are notably limited in spatial resolution. Conversely, electron microspectroscopies provide the highest spatial resolution but lack a high degree of chemical specificity, particularly for organic species. Electron and other high resolution microspectroscopies like scanning transmission X-ray microscopy–near edge X-ray absorption fine structure spectroscopy (STXM-NEXAFS) typically require the sample to be characterized under vacuum, which can appreciably affect particle morphology and composition at the particle vacuum interface. Advancements in ubiquitous techniques like Fourier transform-infrared (FTIR) spectroscopy have culminated with the advent of the discrete-frequency quantum cascade laser (QCL), enabling single-frequency infrared (IR) imaging and faster data acquisition.[6] Notwithstanding advancements, such far-field IR vibrational microspectroscopies lack depth-resolving capabilities and are intrinsically restricted in spatial resolution by the wavelength-dependent diffraction limit of the probing IR light, which is typically between 5 and 12 µm across fingerprint regions and dependent on the particular objective lens used.[7] Efforts to circumvent such diffraction limited resolution have led to recent progress in optical-photothermal infrared (O-PTIR) microspectroscopy techniques, where selective absorbance of mid-IR excitation laser light is detected using a visible light probe laser via a photothermally induced thermal lensing effect.[8–18] In such all-optical schemes, the detectable signal is the modulated probe laser power ΔP_{probe}, which is linearly proportional to

A. J. Wang, Dr. S. Maharjan, Dr. K.-S. Liao, Prof. S. A. Curran
Advanced Manufacturing Institute
University of Houston
Houston, TX 77023, USA
E-mail: awang8@uh.edu

A. J. Wang, Dr. S. Maharjan, Dr. K.-S. Liao, Prof. S. A. Curran,
B. P. McElhenny, Dr. S. Chen
Department of Physics
University of Houston
Houston, TX 77204, USA

E. P. Dillon
Photothermal Spectroscopy Corp
Santa Barbara, CA 93101, USA

B. P. McElhenny, Dr. S. Chen, T. Tong, Dr. J. Bao
Texas Center for Superconductivity
University of Houston
Houston, TX 77204, USA

T. Tong, Dr. J. Bao
Department of Electrical and Computer Engineering
University of Houston
Houston, TX 77204, USA

The ORCID identification number(s) for the author(s) of this article can be found under https://doi.org/10.1002/admi.202001720.

DOI: 10.1002/admi.202001720

both the excitation laser power P_{IR} and probe laser power P_{probe} as well as the number density N of functional groups by the following expression[7]

$$\Delta P_{\mathrm{probe}} \propto \frac{\alpha N}{\kappa C_{\mathrm{p}}}\left(\frac{\partial n}{\partial T}\right) P_{\mathrm{probe}} P_{\mathrm{IR}} \tag{1}$$

where α is the effective absorbance cross-section, κ is the local thermal conductivity, C_{p} is the local heat capacity, n is the local refractive index, and T is the local temperature. Recent success in a tangential technique pairing atomic force microscopy with photothermal infrared deflection spectroscopy (AFM-IR) can resolve vibrational mode variations in 100-nm features, albeit at the expense of data acquisition time, where high-resolution scans can take >20 min to acquire and AFM tip-sample interactions must be considered. The O-PTIR technique reported on in this work is noncontact and utilizes tunable pulsed mid-IR laser light (5.5–12 µm) from a QCL to excite a selected spot on a sample under ambient conditions, measuring IR absorbance through energy and position perturbations in scattered confocal coaxial 532-nm laser light due to localized photothermally induced shifts in refractive index from the sample at laser foci (**Figure 1**a).[7,19,20]

Changes/perturbations in scattered visible light are detected using a lock-in amplifier to extract the modulated IR absorbance signal from the total reflected light. A generalized schematic diagram illustrating the key components of the O-PTIR technique is provided in Figure S1 (Supporting Information). As a corollary to the collinear laser light arrangement, inelastically scattered Stokes-/Anti-Stokes-shifted light may be simultaneously collected and processed to obtain concomitant IR and Raman spectra (O-PTIR+R) from the same local *x*–*y* coordinates, as illustrated with a particle of neat poly(octadecyl acrylate) (PODA) (Figure 1b–e). A high-resolution single-frequency IR image collected at 1738 cm^{-1} to visualize the distribution of carbonyl group moieties across a particle of PODA with a pixel size of 100 nm is shown in Figure 1b along with an optical image (Figure 1c) demarcating where location-specific measurements were collected. The 1738 cm^{-1} band displayed in Figure 1b is normalized to a region of raised baseline at 1628 cm^{-1} (C=C stretching) observed in IR absorbance spectra where PODA-*g*-MWCNTs are present. Characteristic IR absorbance peaks (Figure 1d) at 1738 cm^{-1} (C=O stretching),[21] 1470 cm^{-1} (–CH$_2$– scissoring),[22] and 1173 cm^{-1} (C–O–C valence vibrations, C–O stretching)[2] along with corresponding active Raman bands (Figure 1e) at 2876 cm^{-1} (–CH$_2$–/–CH$_3$ stretching)[2] and 970 cm^{-1} (Si–O stretching)[23] taken at target-specific locations near peripheral and central regions confirm the presence of PODA and the underlying native oxide layer-passivated Si-wafer substrate, which agrees well (98.1%) with Wiley's KnowItAll IR spectral database (Figure S2, Supporting Information) and conventional Raman spectra (Figure S3, Supporting Information) independently collected. O-PTIR+R has very recently been used to characterize depth-resolved molecules in living cells,[7] polymorphic amyloid aggregates in neurons,[24] sub-micrometer atmospheric particulates,[25] pharmaceutical dry-powder aerosols,[26] <10-µm organic contaminants on hard drives,[27] bioplastic composite interfaces,[28] high-explosive trace materials,[29] and Ruddlesden–Popper hybrid perovskite crystals exhibiting peripheral 2D/3D heterostructure formation,[30] which show excellent correlation to conventional FTIR absorbance spectra.

In this work, a human body temperature-sensitized thermometric polymeric nanocomposite of poly(octadecyl acrylate)-grafted-multiwall carbon nanotubes (PODA-*g*-MWCNTs) for wearable temperature sensors recently reported on is characterized using an all-optical O-PTIR+R microspectroscopy technique, resolving interfacial regions with remarkable chemical specificity and a theoretical sub-micrometer resolution of ≈416 nm, as determined by the Rayleigh criterion and objective numerical aperture.[2] This communication is the first report characterizing a conductive nanocarbon-based disordered polymer nanocomposite using the O-PTIR+R technique. Results from this work demonstrate unprecedented chemical specificity across nanometric step size intervals spanning nanocarbon/host–polymer interphases. The PODA-*g*-MWCNTs characterized in this work are synthesized through a RAFT-polymerization scheme and exhibit extraordinarily large, repeatable, electronic switching facilitated through form-stable glass transitions near human fever temperatures and is a promising low-cost candidate material for wearable temperature sensors (Experimental Section, Supporting Information).[2,31] Atomic force microscopy (AFM) topography images, corresponding location-specific AFM-IR spectra, and field-emission electron microscopy images of PODA-*g*-MWCNTs are presented in **Figure 2**. IR photothermal amplitude spectra directly proportional to IR absorbance bands obtained at location-specific target sites (Figure 2b) are presented in Figure 2c,d. Prominent IR absorbance bands at 1737 cm^{-1} (C=O stretching), 1459 cm^{-1} (–CH$_2$– scissoring), and 1171 cm^{-1} (C–O–C valence vibrations, C–O stretching) confirm the presence of PODA while IR bands at 1595 cm^{-1} (C=C stretching)[2,21] from the E_{1u} in-plane mode and 1373 cm^{-1} (disorder band)[2,32] verify the presence of MWCNTs. AFM-IR spectra obtained from off-particle regions (Figure 2d) clearly contrast PODA-*g*-MWCNTs from the Si substrate. A field-emission scanning electron image of PODA-*g*-MWCNTs shows a uniform distribution of interconnected high aspect ratio grafted MWCNTs. High-resolution transmission electron images (Figure 2f–h) resolve the nanostructure of PODA-*g*-MWCNTs as a system of PODA-wrapped MWCNTs, where constricting, bridging, and webbing arrangements are observed. Detailed spectroscopic and electronic characterizations of PODA-*g*-MWCNTs have previously been reported on by Wang et al.[2]

To clearly contrast interfacial regions, PODA-*g*-MWCNT samples were solubilized and sonicated in decane prior to spincoating onto native oxide layer-passivated crystalline Si-wafer substrates to allow any free/unbound PODA to separate from MWCNT-rich regions. False-color single-frequency IR absorbance images with 100-nm pixel size of a particle of PODA-*g*-MWCNTs collected at 1736 cm^{-1}, normalized to a region of raised baseline at 1628 cm^{-1} (C=C stretching), to image the carbonyl groups of PODA-rich regions and at 1628 cm^{-1}, normalized to the 1736 cm^{-1} band, to image C=C stretching vibrations in PODA-*g*-MWCNT-rich regions are presented in **Figure 3**a,b. An optical image (Figure 3c) corresponding to the single-frequency IR maps presented in Figure 3a,b shows a line array of 20 color-coordinated

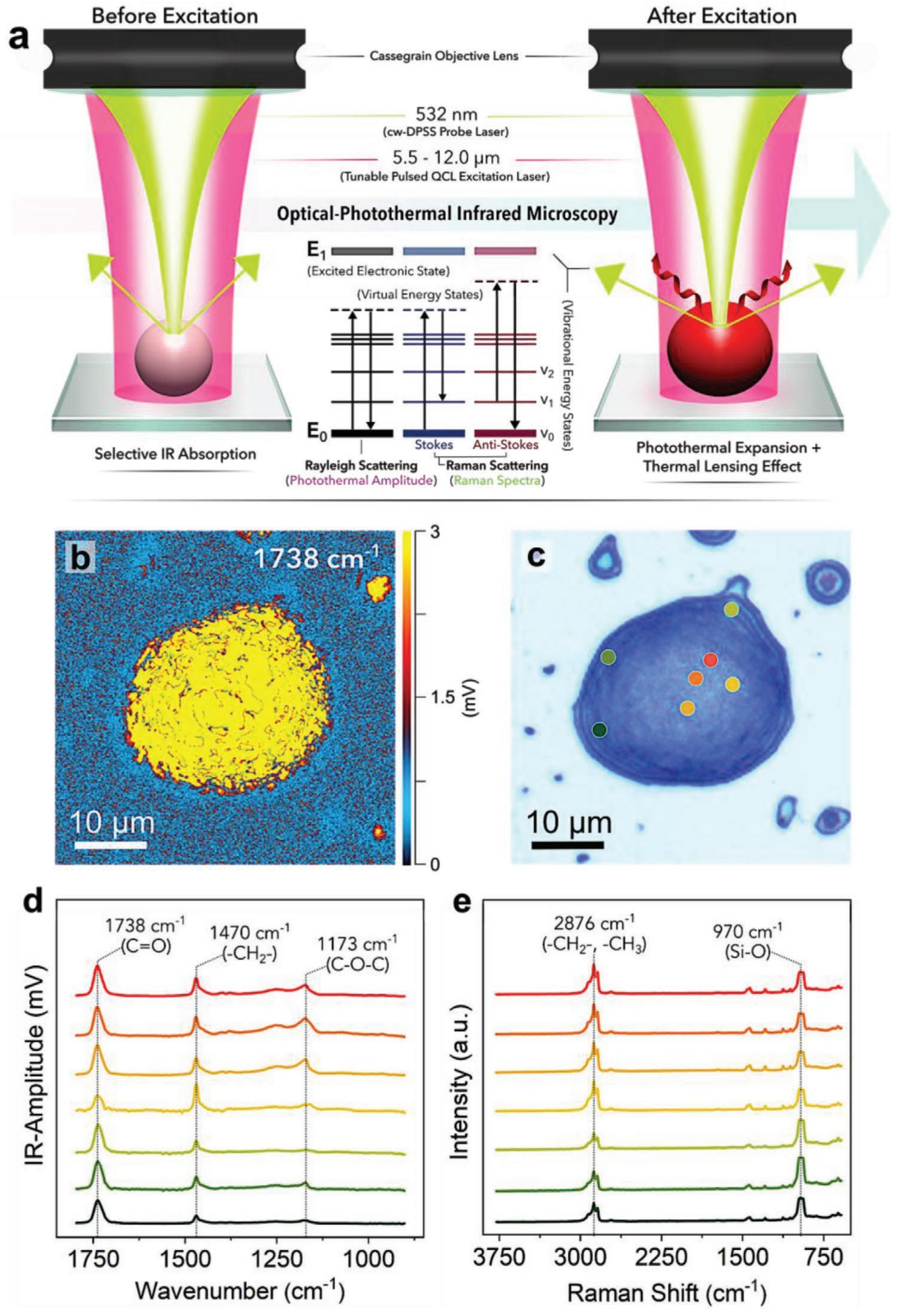

Figure 1. a) Schematic cartoon illustrating the working principle of the optical-photothermal infrared (O-PTIR) spectroscopy technique. b) High-resolution (100 nm pixel size) single-frequency IR absorbance map of neat poly(octadecyl acrylate) collected at 1738 cm^{-1}, baseline normalized to a region of raised baseline at 1628 cm^{-1} (C=C stretching), to image carbonyl groups of acrylate moieties. c) 40× optical image corresponding to panel (b) with overlaid color-coordinated markers denoting where individual region-specific photothermal amplitude spectra were taken. d) Photothermal amplitude spectra taken at location-specific regions demarcated in panel (c) and e) concomitantly obtained corresponding Raman spectra.

markers partitioned into three distinct regions demarcating where simultaneous IR-photothermal amplitude and Raman spectra were obtained at 1.5-μm step-size intervals. IR-photothermal amplitude spectra (Figure 3d–f) across the three regions defined in Figure 3c quantitatively resolve a region of essentially neat PODA (Region 1), a transitional region rich in PODA-*g*-MWCNTs (Region 2), and a transitional region between PODA-*g*-MWCNTs and neat PODA (Region 3). Raised baselines from broadband absorbance and a characteristic region of raised baseline at 1628 cm^{-1} resulting from C=C

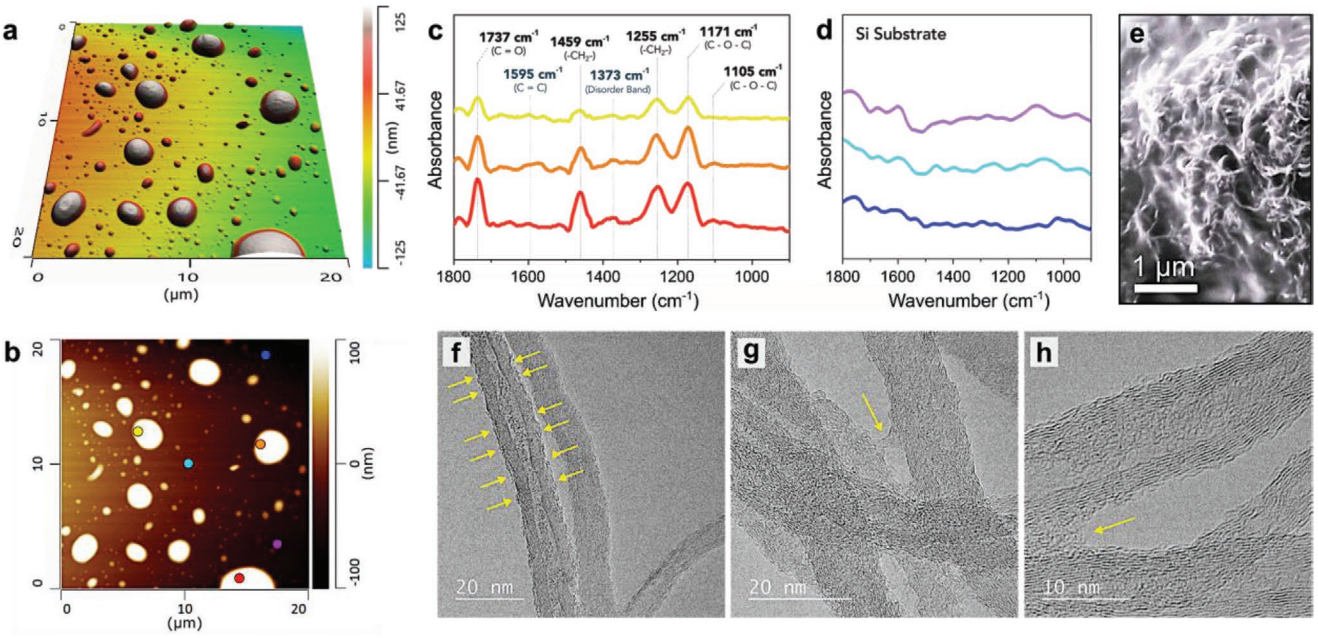

Figure 2. a) False-color 3D AFM topography orthographic projection image of PODA-*g*-MWCNTs and b) its corresponding AFM topography map with overlaid color-coordinated dot markers corresponding to panel (c). Location-specific AFM-IR-absorbance spectra of c) PODA-*g*-MWCNTs and d) the Si substrate, corresponding to panel (b). e) Field-emission scanning electron image of PODA-*g*-MWCNTs. f–h) Field-emission transmission electron microscopy images of PODA-*g*-MWCNTs at different magnifications. The yellow arrows in panels (f)–(h), denote regions where PODA is observed constricting a MWCNT, bridging between MWCNTs, and webbing between MWCNTs, respectively.

stretching verify the presence of MWCNTs across Region 2 (Figure 3e). While raised baselines due to broadband absorbance are not readily evident in stacked spectra (Figure 3), they are clearly observed in an overlapping plot of the raw O-PTIR spectra presented in Figure 3d–i (Figure S4, Supporting Information). Figure 3e,f,h,i shows transitional regions where broadband absorbance from MWCNTs is observed. Semiconducting and metallic MWCNTs exhibit strong electromagnetic absorption between and around the S_{22} and S_{11} excitonic peaks, which makes IR spectroscopy of MWCNTs challenging due to overlapping signals and strong elevated baselines. All sp^2-hybridized allotropes of carbon contrastingly exhibit strong and characteristically discernable Raman spectral features. Because Raman spectra are simultaneously collected from the exact same spot as O-PTIR spectra, Raman can be used as a corroboratory tool to confirm the presence and location of PODA-*g*-MWCNT regions (Figure 3e,h). Without the combined O-PTIR+R approach, it would be challenging to confirm both the chemical composition and locality of such 1D graphitic nanomaterials with precision and certainty.

Raman spectra (Figure 3g–i) concomitantly obtained from the same target sites demarcated in Figure 3c corroborate IR-amplitude spectra across all three regions, where a characteristic active Raman band of PODA at a shift of 2876 cm^{-1} (–CH_2–/–CH_3 stretching) and those of MWCNTs at shifts of 1590 cm^{-1} (G-band) from the E_{2g} optical mode and 1337 cm^{-1} (D-band) clearly differentiate the three regions and agree well with independently obtained Raman spectra (Figure S3, Supporting Information).[21,32] Benefits of the combinatory O-PTIR+R approach are evident when considering baseline fluorescence often present in Raman spectra at shorter excitation wavelengths. Raman spectra collected from regions of neat PODA show strong broadband fluorescence that renders definitive identification via spectral database searches problematic without significant baseline correction (Figure S3, S5, Supporting Information). While challenging for Raman signals, fluorescence does not affect O-PTIR spectra of neat PODA, which show distinctive absorbance peaks devoid of elevated baselines and spectral artifacts. Hence, samples that are difficult to characterize with Raman due to fluorescence, can be measured and characterized with O-PTIR successfully to positively identify PODA with a high hit-quality index (HQI) (Figure S2, Supporting Information). It is worth noting that Raman is often performed at longer excitation wavelengths to minimize fluorescence, albeit at the expense of spectral sensitivity. For instance, increasing the excitation wavelength from 532 to 785 nm decreases the Raman effect by ≈4.7×, thus requiring an ≈22× longer acquisition time to reach comparable spectral sensitivity. In contrast, the sensitivity of O-PTIR spectra is virtually unaffected by probe wavelength. O-PTIR+R spectra and analysis of a second PODA-*g*-MWCNT particle confirm the results presented in Figure 3 (Figure S6, Supporting Information), where 40 contiguous IR-photothermal amplitude and Raman spectra concomitantly collected across an 80-μm line array spanning analogous transitional regions are shown.

Interfacial regions can be further characterized by evaluating fingerprint IR absorbance and Raman band intensities as a function of lateral distance and comparing peak ratio magnitudes (**Figure 4**). IR amplitudes (Figure 4a) and Raman intensities (Figure 4b) with lateral distance, corresponding to Figure 3c, show regions of varying number density

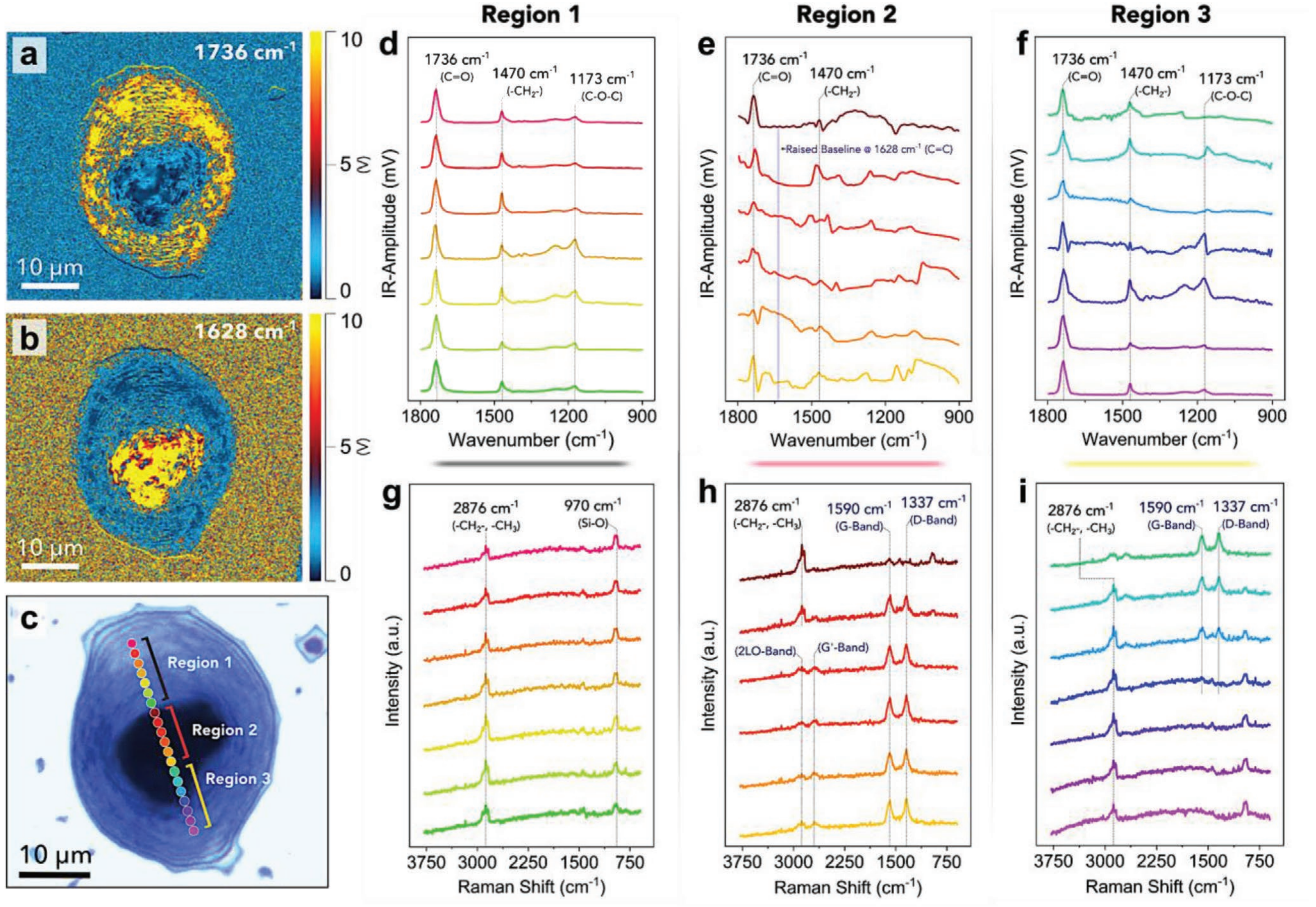

Figure 3. High-resolution (100-nm pixel size) discrete single-frequency IR absorbance maps of PODA-*g*-MWCNTs collected at a) 1736 cm^{-1} to image C=O stretching from carbonyl groups of PODA and b) 1628 cm^{-1} to image C=C stretching from MWCNTs. c) Optical image taken at 40× magnification corresponding to panels (a) and (b) with colored markers demarcating line arrays across nanocomposite interfacial regions obtained at a 1.5-µm step-size interval. Color-coordinated d–f) O-PTIR spectra and g–i) Raman spectra demarcated by the colored line array in panel (c).

of characteristic functional groups. Figure 4a shows variations in IR amplitude intensity with distance for the 1736 and 1628 cm^{-1} absorbance bands, representative of carbonyl groups of PODA and sp^2-hybridized carbon, respectively. Concordantly, Figure 4b shows variations in Raman intensity in the 2876 cm^{-1} (–CH$_2$–/–CH$_3$ stretching) vibrational mode of PODA as well as the 1583 cm^{-1} (G-band) and 1337 cm^{-1} (D-band) vibrational modes of MWCNTs. Inter-region variations along the measured line array from Figure 3c are clearly observed by comparing IR-amplitude (Figure 4c) and Raman intensity (Figure 4d) peak ratios. Peak ratios of 1628 cm^{-1}/1736 cm^{-1} for IR-amplitudes and 1583 cm^{-1}/2876 cm^{-1} for Raman intensities are shown, both representative of MWCNT-rich regions (Figure 4c,d). Figure 4c shows the IR-amplitude peak ratio (1628 cm^{-1}/1736 cm^{-1}) representative of C=C stretching jump from 0.014 in Region 1 to as high as 0.918 in Region 2, a percent-increase of 6459%, which agrees well with corresponding Raman intensity peak ratios (Figure 4d). As more complex nanocomposite systems are realized and evolve, so does the role of standardized computational spectral databases and search software to spectroscopically identify components with precision and confidence. Spectral database search algorithms typically rank the degree of correlation between an unknown spectrum and a reference spectrum using an HQI. An HQI is assigned to each candidate reference spectrum and is a metric for how closely a reference spectrum matches the unknown spectrum – a better match corresponds to a higher HQI. Multidimensional analysis database searches using complementary vibrational spectroscopy techniques like Raman and IR obtained simultaneously via O-PTIR+R from the same spot and sub-micrometer resolution improve the accuracy of spectral identification/verification beyond the capabilities of conventional vibrational spectroscopies and minimize experimental uncertainty. Figure 4e shows a 2D graphical representation of the IR spectral HQI plotted against the corresponding Raman spectral HQI of a region of neat PODA using Wiley's KnowItAll, where a strong correlation is observed between the two techniques as evidenced by the closely clustered dual search hits. Candidate spectra are required to exist for all generated hits (i.e., each hit corresponds to a unique pair of IR and Raman spectra for the same candidate structure). A high quality hit in Figure 4e is a close match corresponding to a poly(ethylene glycol) (PEG) distearate under the general class of polyacrylic and polymethacrylic esters. While PODA does not include a PEG backbone, it does exhibit the same esters of stearic acid

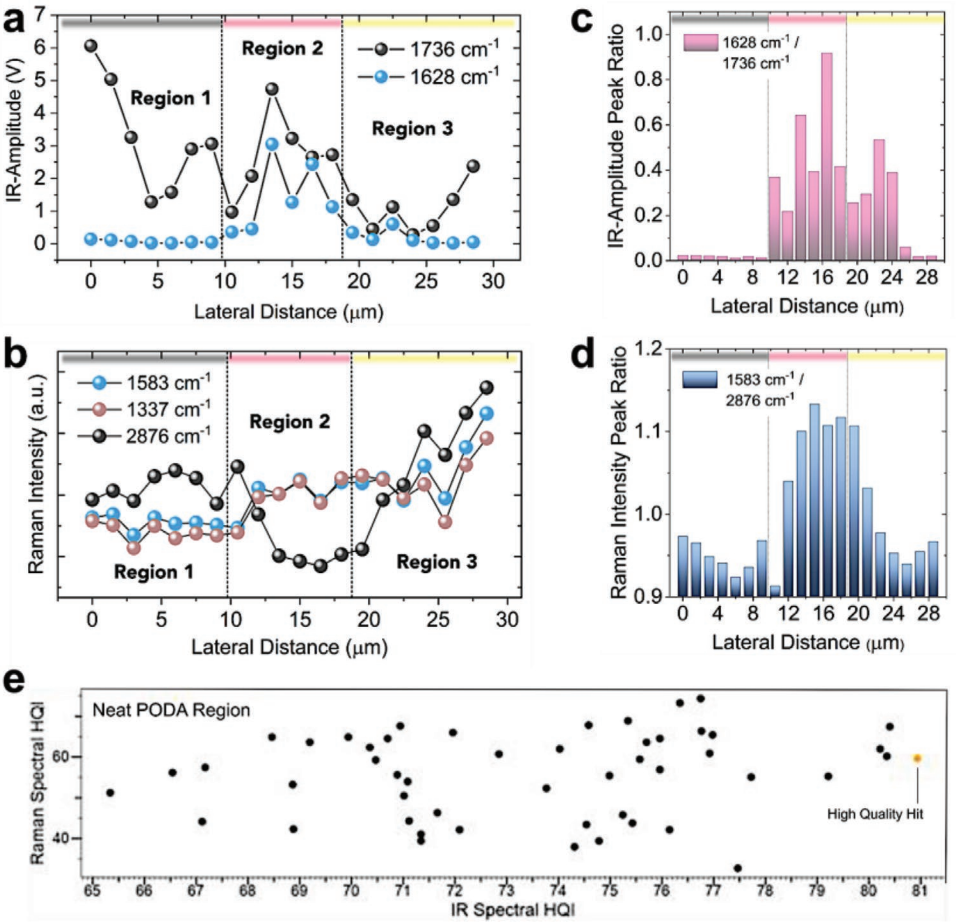

Figure 4. a) IR-amplitude magnitudes of absorbance bands 1736 cm^{-1} (C=O stretching) and 1628 cm^{-1} (C=C stretching) and b) corresponding Raman intensity magnitudes at shifts of 1583 cm^{-1} (G-band), 1337 cm^{-1} (D-band), and 2876 cm^{-1} (–CH$_2$–/–CH$_3$ stretching) of PODA-*g*-MWCNTs partitioned by region, in reference to Figure 3, and obtained at 1.5-µm step-size intervals. c) IR-amplitude peak ratios (1628 cm^{-1}/1736 cm^{-1}) and d) corresponding Raman intensity peak ratios (1583 cm^{-1}/2876 cm^{-1}) as a function of lateral distance corresponding to panels (a,b). The black, red, and yellow headers demarcate the different regions defined in Figure 3c. e) Scatter plot of the hit-quality index (HQI) of Raman spectra against IR spectra from a region of neat PODA using Wiley's KnowItAll spectral database. A high-quality hit is demarcated in yellow on the far right.

and repeating, adjoining methylene backbone groups, strongly supporting the presence of PODA. Because O-PTIR+R spectra are simultaneously collected from the exact same locality at the same spatial resolution, 2D HQI plots provide a more powerful means by which to accurately identify organic species from multi-dimensional hit list libraries with sub-micrometer spatial precision, a feat unobtainable by means of ordinary Raman or FTIR/QCL spectroscopy alone.

Complementing discrete-frequency IR imaging, the O-PTIR+R technique utilized in this work also affords hyperspectral Raman imaging with the same sub-micrometer spatial resolution as discrete-frequency O-PTIR images (Figure 3), providing further supporting high-resolution spectral evidence (**Figure 5**). Raman images from hyperspectral data of a PODA-*g*-MWCNT particle displayed at a shift of 1583 cm^{-1} (G-band), normalized to the 2876 cm^{-1} (–CH$_2$–/–CH$_3$ stretching) mode, show concentrated discrete regions of MWCNTs (Figure 5a), while the image displayed at a shift of 2876 cm^{-1}, normalized to the 1583 cm^{-1} mode, show alkyl- and methyl-rich moieties of PODA (Figure 5b). The crosshair reticles overlaid atop the hyperspectral Raman maps (Figure 5a,b) demarcate where representative individual point Raman spectra were collected, as shown in the corresponding optical image (Figure 5c). The *x*–*y* coordinates listed by each reticle are the global coordinates within each respective image. Raman spectra color-coordinated with the red and gold markers in Figure 5c uniquely identify the dissimilar regions/phases (Figure 5d). A hyperspectral Raman image displayed at a shift of 520 cm^{-1}, normalized to the 2876 cm^{-1} mode, to image the Si-wafer substrate corroborates Figure 5a,b, where the substrate clearly outlines the peripheral of the PODA-*g*-MWCNT particle (Figure S7, Supporting Information). After repeated and prolonged beam exposure to pulsed mid-IR QCL and 532-nm diode lasers at high powers while acquiring high-resolution single-frequency O-PTIR maps, minor sample damage was observed (Figure S8, Supporting Information), however this was not a common artifact. A data acquisition time of ≈1 s per O-PTIR+R spectrum was typical, yielding super-resolution transmission quality IR absorbance spectra profiles with simultaneous Raman intensity spectra through a noncontact all-optical technique.

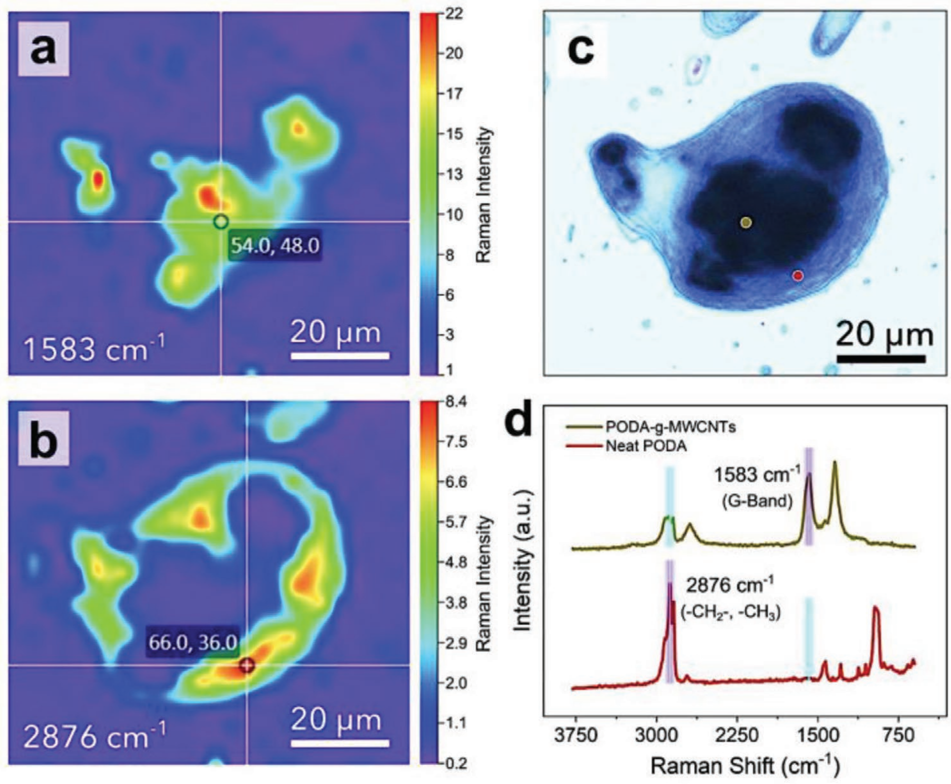

Figure 5. False-color hyperspectral Raman maps of PODA-*g*-MWCNTs displayed a) at a shift of 1583 cm^{-1}, normalized to the 2876 cm^{-1} band, to image C=C stretching in MWCNTs and b) at a shift of 2876 cm^{-1}, normalized to the 1583 cm^{-1} band, to image the methylene and methyl groups of poly(octadecyl acrylate). c) 40× magnification optical image corresponding to panels (a) and (b), where the color markers demarcate where Raman point spectra were collected, corresponding to panels (a–c). d) Raman spectra collected at the colored-coordinated markers in panel (c), where purple and magenta lines demarcate characteristic Raman bands used to form panels (a,b).

In summary, we report on the first characterization of a disordered nanocarbon-based polymer nanocomposite across interfacial regions using an all-optical super-resolution hyperspectral O-PTIR+R microspectroscopy technique under ambient conditions. Location-specific reflection-mode IR photothermal amplitude spectra well-correlated to traditional transmission-mode FTIR absorbance spectra with concomitantly obtained Raman spectra collected with sub-micrometer wavelength-independent spatial resolution demonstrate unprecedented combined spatial and chemical specificity. Distribution and density of discrete functional groups across heterogeneous nanocomposite interphases are resolved without dispersive spectral artifacts from wavelength-dependent scattering as would be seen in conventional FTIR/QCL microspectroscopy. Interfacial regions within interphases of nanocomposite particles of PODA-*g*-MWCNTs are spectroscopically resolved well beyond the limitations of conventional IR spectroscopies as regions rich in neat PODA, regions concentrated with PODA-*g*-MWCNTs, transitional regions, and regions of bare substrate. This Communication demonstrates a complementary and corroboratory vibrational microspectroscopy technique that can accurately identify organic species with sub-micrometer spatial and chemical precision. We show how the O-PTIR+R technique is used to confirm both the chemical composition and locality of PODA-*g*-MWCNTs with confidence, spatial precision, and chemical specificity. Results from this work may be extrapolated to other nanocomposite systems where discrete-frequency imaging of interfacial or edge-boundary regions with chemical exactitude is requisite towards a more quantitative insightful understanding of nano-, meso-, and microscale interphases.

Supporting Information

Supporting Information is available from the Wiley Online Library or from the author.

Acknowledgements

S.C. acknowledges support from the State of Texas through the Texas Center for Superconductivity at the University of Houston. J.B. acknowledges support from the Robert A. Welch Foundation (E-1728). The authors thank Dr. Mustafa Kansiz and Jay Anderson for insightful discussions on the O-PTIR+R technique. The authors acknowledge the anonymous Reviewer, whose comments/suggestions improved the overall quality of the work.

Conflict of Interest

The authors declare no conflict of interest.

Keywords

hyperspectral, nanocomposite interfaces, photothermal, Raman spectroscopy, super-resolution infrared spectroscopy

Received: September 30, 2020
Revised: December 6, 2020

---

[1] A. J. Wang, K.-S. Liao, S. Maharjan, Z. Zhu, B. McElhenny, J. Bao, S. A. Curran, *Nanoscale* **2019**, *11*, 8565.
[2] A. J. Wang, S. Maharjan, K.-S. Liao, B. P. McElhenny, K. D. Wright, E. P. Dillon, R. Neupane, Z. Zhu, S. Chen, A. R. Barron, *ACS Appl. Nano Mater.* **2020**, *3*, 2288.
[3] J. R. Potts, D. R. Dreyer, C. W. Bielawski, R. S. Ruoff, *Polymer* **2011**, *52*, 5.
[4] M. Moniruzzaman, K. I. Winey, *Macromolecules* **2006**, *39*, 5194.
[5] J. Horne, L. McLoughlin, E. Bury, A. S. Koh, E. K. Wujcik, *Adv. Mater. Interfaces* **2020**, *7*, 1901851.
[6] M. R. Kole, R. K. Reddy, M. V. Schulmerich, M. K. Gelber, R. Bhargava, *Anal. Chem.* **2012**, *84*, 10366.
[7] D. Zhang, C. Li, C. Zhang, M. N. Slipchenko, G. Eakins, J.-X. Cheng, *Sci. Adv.* **2016**, *2*, e1600521.
[8] D. Fournier, F. Lepoutre, A. Boccara, *J. Phys. Colloq.* **1983**, *44*, C6.
[9] M. Harada, K. Iwamoto, T. Kitamori, T. Sawada, *Anal. Chem.* **1993**, *65*, 2938.
[10] D. Lasne, G. A. Blab, F. De Giorgi, F. Ichas, B. Lounis, L. Cognet, *Opt. Express* **2007**, *15*, 14184.
[11] D. Boyer, P. Tamarat, A. Maali, B. Lounis, M. Orrit, *Science* **2002**, *297*, 1160.
[12] A. Gaiduk, M. Yorulmaz, P. Ruijgrok, M. Orrit, *Science* **2010**, *330*, 353.
[13] R. Furstenberg, C. Kendziora, M. Papantonakis, V. Nguyen, R. A. McGill, Chemical imaging using infrared photothermal microspectroscopy, Vol. *8374*, SPIE **2012**.
[14] A. Mërtiri, T. Jeys, V. Liberman, M. Hong, J. Mertz, H. Altug, S. Erramilli, *Appl. Phys. Lett.* **2012**, *101*, 044101.
[15] R. Sullenberger, S. Redmond, D. Crompton, A. Stolyarov, W. Herzog, *Opt. Lett.* **2017**, *42*, 203.
[16] Z. Li, K. Aleshire, M. Kuno, G. V. Hartland, *J. Phys. Chem. B* **2017**, *121*, 8838.
[17] C. Li, D. Zhang, M. N. Slipchenko, J.-X. Cheng, *Anal. Chem.* **2017**, *89*, 4863.
[18] Y. Wang, Y. Tang, P. Cheng, X. Zhou, Z. Zhu, Z. Liu, D. Liu, Z. Wang, J. Bao, *Nanoscale* **2017**, *9*, 3547.
[19] G. Busse, *Opt. Commun.* **1981**, *36*, 441.
[20] A. Dazzi, F. Glotin, R. Carminati, *J. Appl. Phys.* **2010**, *107*, 124519.
[21] Z. Liu, X. Lu, P. Peng, W. Wu, S.-S. Pei, Q. Yu, J. Bao, *Phys. Rev. B* **2010**, *82*, 155435.
[22] Z. Zhu, V. G. Hadjiev, Y. Rong, R. Guo, B. Cao, Z. Tang, F. Qin, Y. Li, Y. Wang, F. Hao, *Chem. Mater.* **2016**, *28*, 7385.
[23] A. K. Yadav, P. Singh, *RSC Adv.* **2015**, *5*, 67583.
[24] O. Klementieva, C. Sandt, I. Martinsson, M. Kansiz, G. K. Gouras, F. Borondics, *Adv. Sci.* **2020**, *7*, 1903004.
[25] N. E. Olson, Y. Xiao, Z. Lei, A. P. Ault, *Anal. Chem.* **2020**, *92*, 9932.
[26] D. Khanal, J. Zhang, W.-R. Ke, M. M. Banaszak Holl, H.-K. Chan, *Anal. Chem.* **2020**, *92*, 8323.
[27] M. Kansiz, C. Prater, E. Dillon, M. Lo, J. Anderson, C. Marcott, A. Demissie, Y. Chen, G. Kunkel, *Microsc. Today* **2020**, *28*, 26.
[28] C. Marcott, M. Kansiz, E. Dillon, D. Cook, M. N. Mang, I. Noda, *J. Mol. Struct.* **2020**, *1210*, 128045.
[29] A. Banas, K. Banas, M. K. F. Lo, M. Kansiz, S. M. P. Kalaiselvi, S. K. Lim, J. Loke, M. B. H. Breese, *Anal. Chem.* **2020**, *92*, 9649.
[30] Z. Qin, S. Dai, C. C. Gajjela, C. Wang, V. G. Hadjiev, G. Yang, J. Li, X. Zhong, Z. Tang, Y. Yao, A. M. Guloy, R. Reddy, D. Mayerich, L. Deng, Q. Yu, G. Feng, H. A. Calderon, F. C. Robles Hernandez, Z. M. Wang, J. Bao, *Chem. Mater.* **2020**, *32*, 5009.
[31] C. Sealy, *Nano Today* **2020**, *32*, 100875.
[32] R. Kostić, M. Mirić, T. Radić, M. Radović, R. Gajić, Z. Popović, *Acta Phys. Pol. A* **2009**, *116*, 718.